RSC Advances

PAPER

View Article Online
View Journal | View Issue

Check for updates

Cite this: *RSC Adv.*, 2026, **16**, 25067

Photo-immunotherapeutic PDA-Ce6-R837 nanoparticles enhance the induction of immunogenic responses in melanoma cells

Jianv Wang, †[a] Chenxi Liu,†[a] Xiaoyan Zhang,†[ab] Yao Xie,[a] Xueyu Zhang,[a] Tingting Wang[a] and Lin Wang*[a]

Received 6th March 2026
Accepted 24th April 2026

DOI: 10.1039/d6ra01921h

rsc.li/rsc-advances

Melanoma is a highly aggressive malignancy characterized by limited immunogenicity and pronounced immune evasion, which represent significant obstacles to effective therapeutic intervention. Building on our previously developed multifunctional PDA-Ce6-R837 nanoparticles (NPs), which have demonstrated favorable antitumor efficacy in squamous cell carcinoma (SCC) models, the present study shifts focus toward elucidating their underlying photo-immunological mechanisms in melanoma cells. Here, we investigate their antitumor and immunoregulatory effects in melanoma cell models. *In vitro* studies demonstrated the efficient internalization of PDA-Ce6-R837 NPs by SK-Mel-28 and A375 cells, which was accompanied by pronounced photothermal and photodynamic responses. Functional assays revealed that this treatment markedly suppressed cell migration and invasion and, under dual-wavelength laser irradiation, significantly induced apoptosis while promoting key hallmarks of immunogenic cell death (ICD), including the translocation of calreticulin (CRT) and the extracellular release of adenosine triphosphate (ATP) and high-mobility group box 1 (HMGB1). In coculture systems, treatment with R837 alone promoted the maturation of bone marrow-derived dendritic cells (BMDCs), whereas laser activation of PDA-Ce6-R837 NPs enhanced BMDC maturation, as evidenced by further upregulation of CD80/CD86 expression and increased IL-12p70 production. Collectively, these findings demonstrate that PDA-Ce6-R837 NPs combine direct cytotoxic effects with immune stimulation in melanoma phototherapy, offering experimental evidence to support the development of phototherapy-based immunotherapeutic strategies for melanoma.

1. Introduction

Melanoma is a highly aggressive skin cancer arising from melanocytes and accounts for approximately 5% of all diagnosed skin cancer cases.[1] In recent years, the global incidence of melanoma has increased substantially; owing to its marked invasiveness and high metastatic potential, it has become a leading cause of skin cancer-related mortality.[2] At the molecular level, melanoma is characterized by a high mutational burden, accompanied by extensive genetic alterations that occur during tumor initiation and progression. These alterations lead to the generation of numerous neoantigens, thereby conferring pronounced immunogenicity upon melanoma cells.[3] This biological feature provides a compelling rationale for the implementation of immunotherapy, which is designed to augment antitumor immune responses and facilitate tumor cell elimination. The advent of immune checkpoint blockade (ICB) has constituted a major breakthrough in melanoma therapy, with significant improvements in survival outcomes and the induction of durable responses observed in a subset of patients.[4,5] However, clinical benefits are not universally observed, as approximately 50% of patients fail to achieve sustained long-term responses.[6] This limitation is largely attributed to the heterogeneity of the tumor immune microenvironment and the presence of diverse immune evasion mechanisms,[3,7] thereby underscoring the urgent need for more effective immunotherapeutic strategies.

Immunogenic cell death (ICD) is a distinct form of regulated cell death that elicits potent antitumor immune activation and is recognized as a pivotal mechanism in cancer immunotherapy.[8] Unlike nonimmunogenic cell death, ICD is characterized by coordinated cellular stress responses and organelle dysfunction, which result in the exposure, secretion, or release of damage-associated molecular patterns (DAMPs).[9,10] Canonical DAMPs include the surface translocation of calreticulin (CRT), the extracellular release of adenosine triphosphate (ATP), and the liberation of high-mobility group box 1 (HMGB1)

---

[a] *Department of Dermatology, West China Hospital, Sichuan University, Chengdu 610041, China. E-mail: lkzwl@126.com*

[b] *Department of Dermatology, West China Second University Hospital, Sichuan University, Key Laboratory of Birth Defects and Related Diseases of Women and Children (Sichuan University), Ministry of Education, Sichuan, 610041, China*

† These authors have contributed equally to this work.

during the process of cell death.[11] These signals serve as potent immunostimulatory cues that are recognized by pattern recognition receptors (PRRs) expressed on dendritic cells (DCs), thereby facilitating tumor antigen uptake, cross-presentation, and the priming of tumor-specific cytotoxic T lymphocytes.[12] Through these mechanisms, ICD contributes to the reprogramming of the tumor immune microenvironment by converting immunologically "cold" tumors, which exhibit limited immune infiltration, into "hot" tumors characterized by enhanced immune cell recruitment and proinflammatory signaling, ultimately improving responsiveness to immunotherapy.[13,14] However, the spontaneous induction of ICD within the tumor microenvironment (TME) is frequently suppressed by immunosuppressive networks composed of regulatory T cells (Tregs), M2-polarized tumor-associated macrophages (M2 TAMs), and myeloid-derived suppressor cells (MDSCs), thereby limiting overall therapeutic efficacy.[15,16] Therefore, strategies that effectively induce or enhance ICD may overcome tumor-associated immunosuppression and enhance the efficacy of cancer immunotherapy.

Photothermal therapy (PTT) is based on the use of photothermal agents that convert near-infrared (NIR) light into localized thermal energy, thereby enabling precise tumor ablation while minimizing damage to surrounding normal tissues.[17–19] Among these agents, polydopamine (PDA) nanoparticles have attracted considerable attention owing to their high photothermal conversion efficiency, excellent biocompatibility and biodegradability, as well as their substantial drug-loading capacity, which enables controlled release in response to endogenous or exogenous stimuli.[20–22] Photodynamic therapy (PDT) is mediated by photosensitizers that, upon irradiation at specific wavelengths, generate singlet oxygen ($^1O_2$) and other reactive oxygen species (ROS), ultimately resulting in tumor cell damage and death.[23,24] Clinically, PDT has been widely applied in the treatment of various malignant and nonmalignant conditions, demonstrating favorable safety profiles and minimal adverse effects.[25–27] The therapeutic efficacy of PDT is determined by multiple factors, including light wavelength, photosensitizer characteristics, and local oxygen availability.[28] New-generation chlorin-based photosensitizers, such as chlorin e6 (Ce6), have been shown to exhibit enhanced tissue penetration within the 650–700 nm therapeutic window.[29] However, the intrinsic hydrophobicity of Ce6 restricts its systemic circulation and tumor-targeted accumulation, thereby limiting its therapeutic potential.[30] As a result, the incorporation of Ce6 into PDA-based nanocarriers has emerged as an effective strategy to improve its aqueous dispersibility and enhance tumor accumulation. Both PDT and PTT not only directly eradicate tumor cells but also induce ICD, thereby promoting the release of DAMPs that activate adaptive immune responses, facilitate TME remodeling, and partially overcome therapeutic resistance.[31,32] However, when applied as monotherapies, PDT is frequently compromised by tumor hypoxia, whereas PTT may be limited by heterogeneous heat distribution and potential off-target thermal injury.[33] Notably, these two modalities exhibit strong complementarity: PTT has been reported to improve tumor oxygenation and enhance photosensitizer delivery, whereas PDT can sensitize tumor cells to hyperthermia, collectively resulting in superior therapeutic efficacy.[34,35] Building upon these combined effects, the integration of PDT/PTT with immunomodulatory agents, such as immune adjuvants or immune checkpoint inhibitors, has been demonstrated to further amplify antitumor immunity and represents a promising strategy for achieving durable local and systemic therapeutic responses.[36,37]

Imiquimod (R837) is a synthetic small-molecule immunomodulator that functions as a potent agonist of toll-like receptors 7 and 8 (TLR7/8), thereby eliciting potent activation of both innate and adaptive immune responses.[38] Upon engagement of TLR7/8, R837 has been shown to stimulate monocytes/macrophages, dendritic cells (DCs), and other immune cell subsets to secrete key proinflammatory cytokines, including interferon-α (IFN-α), tumor necrosis factor-α (TNF-α), and interleukin-12 (IL-12), thereby enhancing antiviral and antitumor immune responses.[39,40] Topical administration of R837 has been demonstrated to promote the maturation and lymph node trafficking of epidermal antigen-presenting cells, resulting in enhanced antigen-specific T-cell priming and activation. In addition to its immunostimulatory properties, R837 has also been reported to directly induce tumor cell apoptosis at high concentrations through TLR7-independent pathways.[41,42] Clinically, a 5% R837 cream has been approved for the treatment of several dermatological malignancies;[43] however, its broader oncological application remains limited due to transient immune activation, insufficient immunological memory, local inflammatory toxicity, and unfavorable physicochemical characteristics.[44,45] These limitations highlight the necessity for the development of advanced delivery strategies to fully harness the therapeutic potential of R837.

In our previous work, multifunctional PDA-Ce6-R837 nanoparticles (NPs) were developed, in which PDA was employed as a carrier for the co-delivery of the photosensitizer Ce6 and the immune adjuvant R837. Upon dual-modal NIR laser irradiation, this system was capable of simultaneously activating photodynamic and photothermal effects while enabling stimulus-responsive drug release.[46] Both *in vitro* and *in vivo* studies have demonstrated that PDA-Ce6-R837 NPs exhibit potent antitumor efficacy and favorable biosafety profiles in squamous cell carcinoma (SCC) models, thereby underscoring their potential to enhance therapeutic outcomes through immune modulation.[46] Despite these encouraging findings, the molecular mechanisms underlying ICD induction by this multimodal nanoplatform and its subsequent orchestration of antitumor immunity remain incompletely elucidated, and its therapeutic relevance in highly immunosuppressive malignancies, such as melanoma, has not yet been established. Therefore, the present study does not aim to develop a new nanomaterial system. Instead, we focus on further elucidating the photo-immunological mechanisms of this established nanoplatform. We applied PDA-Ce6-R837 NPs in melanoma cell models to perform a systematic *in vitro* evaluation of their antitumor efficacy, with particular emphasis on their capacity to induce ICD and promote DCs maturation. This study aims to provide preliminary *in vitro* insight into the photo-immunological effects of this nanoplatform and experimental evidence for further investigation of phototherapy-based immunotherapeutic strategies.

2. Materials and methods

2.1 Materials and chemicals

Dopamine hydrochloride, R837, Tris, and dimethyl sulfoxide (DMSO) were purchased from Sigma-Aldrich (USA). Ce6 was obtained from J&K Scientific (Beijing, China). DMEM, RPMI 1640 and trypsin–EDTA were obtained from Gibco (USA). Fetal bovine serum (FBS) and penicillin–streptomycin were from Hyclone (USA). CCK-8 assay kits were purchased from Dojindo (Japan). Matrigel® was obtained from BD Biosciences (USA), and 4% paraformaldehyde from Biosharp (Hefei, China). Primary antibodies, including FITC anti-mouse CD11c, APC anti-mouse CD80, and PE anti-mouse CD86, were obtained from BioLegend (USA), while anti-CRT was obtained from Affinity Biosciences (Jiangsu, China). Secondary antibodies and blocking reagents were obtained from Biosynthesis Biotechnology (Beijing, China). ELISA detection kits for HMGB 1 and ATP Assay Kit were obtained from ZCIBIO Technology (Shanghai, China), and IL-12p70 ELISA kits were from Lianke Biotechnology (Hangzhou, China).

2.2 Synthesis and characterization of PDA-Ce6-R837 NPs

The PDA-Ce6-R837 NPs used in this study were from the same batch as previously reported.[46] Briefly, PDA NPs were prepared *via* dopamine self-polymerization in alkaline Tris buffer. PDA-Ce6-R837 NPs were obtained by incubating PDA NPs with Ce6 and R837 under stirring for 48 h. The morphology of the nanoparticles was characterized by transmission electron microscopy (TEM, FEI Talos F200S G2, USA) and field-emission scanning electron microscopy (SEM, JEOL, Japan). For TEM analysis, samples were dispersed in deionized water, dropped onto carbon-coated copper grids, and dried prior to imaging. For SEM observation, samples were deposited onto substrates and sputter-coated before measurement. Ultraviolet-visible (UV-Vis) absorption spectra were recorded using a UV-Vis spectrophotometer (TA Instruments, USA). Fourier transform infrared (FTIR) spectra were obtained using a Nicolet IS5 spectrometer (Thermo Scientific, USA) with the KBr pellet method. X-ray photoelectron spectroscopy (XPS) was performed on a K-Alpha spectrometer (Thermo Fisher Scientific, USA). The hydrodynamic size were measured by dynamic light scattering (DLS) using a Zetasizer Nano ZS instrument (Malvern, UK).

2.3 Encapsulation efficiency and loading efficiency of PDA-Ce6-R837 NPs

The encapsulation efficiency (EE) and loading efficiency (LE) of Ce6 and R837 in PDA-Ce6-R837 NPs were determined by measuring the amount of unencapsulated drug using UV-Vis spectroscopy. Briefly, the nanoparticle suspension was centrifuged to separate the supernatant, and the concentration of free Ce6 and R837 in the supernatant was quantified. The EE and LE were calculated according to the following equations:

$$\text{EE}\ (\%) = [(W_0 - W_f)/W_0] \times 100\%;\ \text{LE}\ (\%) = [(W_0 - W_f)/W_{\text{NPs}}] \times 100\%$$

where W_0 is the initial amount of Ce6 or R837 added, W_f is the amount of free (unencapsulated) drug in the supernatant, and W_{NPs} is the total mass of nanoparticles.

2.4 Release of Ce6 and R837 *in vitro*

The release profiles of Ce6 and R837 from PDA-Ce6-R837 NPs were systematically evaluated using a dialysis-based approach. Briefly, PDA-Ce6-R837 NPs suspensions (1 mL, 10 mg mL^{-1}) were sealed within dialysis membranes (3500 Da) and immersed in PBS, followed by incubation at 37 °C under continuous agitation in the dark. For laser-stimulated conditions, samples were exposed to 808 nm irradiation (1 W cm^{-2}, 5 min) prior to each sampling point. At defined intervals, aliquots of the external medium were collected for quantitative analysis of Ce6 and R837, with fresh PBS replenished to maintain constant volume. Cumulative release was calculated based on measured concentrations and presented as time-dependent release profiles.

2.5 Photothermal properties *in vitro*

The photothermal stability of PDA-Ce6-R837 NPs solutions (1000 μg mL^{-1}) was evaluated under on/off laser irradiation cycles (1 W cm^{-2}, three cycles, 10 min per cycle). The temperature elevation and cooling processes were continuously recorded using an infrared thermal imaging camera. In addition, the photothermal conversion efficiency (η) was calculated according to previously reported methods.[47,48] The formula used for the calculation is given below.

$$\eta = \frac{hs(T_{\max} - T_{\text{surr}}) - Q_{\text{dis}}}{I\left(1 - 10^{-A_{808}}\right)}$$

$$hs = \frac{m_i C_{\text{H}_2\text{O}}}{\tau_s}$$

$$Q_{\text{dis}} = hs(T_{\max,\text{H}_2\text{O}} - T_{\text{surr}})$$

$$t = -\tau_s \ln(\theta)$$

$$\theta = \frac{T - T_{\text{surr}}}{T_{\max} - T_{\text{surr}}}$$

where h is the thermal conductivity coefficient; s is the laser irradiation area; $T_{\max}$ is the maximum equilibrium temperature; T_{surr} is the surrounding ambient temperature; Q_{dis} is the thermal dissipation value of the solvent and container; I represents the laser power; and A_{808} represents the absorbance of dye at a wavelength of 808 nm. m_i represents the mass of deionized water; C_{H2O} is the heat capacity of deionized water (4.2 J g^{-1}).

2.6 Cell culture

Human melanoma A375 and SK-Mel-28 cell lines were obtained from Procell (Wuhan, China). A375 cells were cultured in DMEM, whereas SK-Mel-28 cells were maintained in RPMI 1640. Complete culture media were prepared by supplementing the basal media with 10% FBS and 1% penicillin–streptomycin. Cells were maintained at 37 °C in a humidified atmosphere containing 5% CO_2 and harvested by detachment using 0.25% trypsin–EDTA.

2.7 Cellular uptake of PDA-Ce6-R837 NPs

A375 and SK-Mel-28 cells (1×10^5 cells per mL) were seeded onto glass-bottom confocal dishes and allowed to adhere overnight. Cells were then incubated with PDA-Ce6-R837 NPs (200 $\mu g\ mL^{-1}$) for 4 h. After washing with PBS to remove uninternalized NPs, cells were fixed with 4% paraformaldehyde and stained with DAPI. Intracellular nanoparticle uptake was visualized by laser scanning confocal microscopy (Zeiss, Germany).

2.8 CCK-8 assays

A375 and SK-Mel-28 melanoma cells were seeded in 96-well plates at 5×10^4 cells per mL and treated with respective drug concentrations (non-irradiated: 0–500 $\mu g\ mL^{-1}$; laser-irradiated: A375, 30–120 $\mu g\ mL^{-1}$; SK-Mel-28, 15–60 $\mu g\ mL^{-1}$). Laser groups were irradiated sequentially with 808 nm (60 s, 1 W cm^{-2}) and 660 nm (30 s, 0.05 W cm^{-2}). The irradiation parameters were selected based on our previous study, in which the photothermal and photodynamic effects of PDA and Ce6 were systematically optimized and validated.[46] Cells were then incubated overnight. Wells were washed with PBS, incubated with 10 μL CCK-8 reagent for 1 h, and absorbance measured using a microplate tester (Thermo Scientific, USA) at 450 nm. Cell viability was calculated as: cell viability (%) = $(OD_{treatment}/OD_{Control}) \times 100\%$.

2.9 ROS detection assays

A375 and SK-Mel-28 melanoma cells were seeded in 12-well plates at 1×10^5 cells per mL and incubated overnight. Cells were assigned to Control (no treatment, no irradiation), laser (irradiation only), PDA-Ce6-R837 NPs, and PDA-Ce6-R837 NPs + laser groups, with drug concentrations of 60 $\mu g\ mL^{-1}$ for A375 and 30 $\mu g\ mL^{-1}$ for SK-Mel-28. After 4 h incubation with the respective treatments, cells were washed twice with PBS and stained with DCFH-DA for 30 min, followed by PBS washes. Laser groups and PDA-Ce6-R837 NPs + laser groups were sequentially irradiated with 808 nm (60 s, 1 W cm^{-2}) and 660 nm (30 s, 0.05 W cm^{-2}) lasers. ROS generation was visualized using an inverted fluorescence microscope (Zeiss, Germany), and images were quantified for mean fluorescence intensity using Image J for statistical analysis.

2.10 Wound healing assays

A375 and SK-Mel-28 cells were seeded in 6-well plates (2×10^5 cells per mL) and incubated overnight. Cells were assigned to Control (no treatment, no irradiation), laser (irradiation only), PDA-Ce6-R837 NPs, and PDA-Ce6-R837 NPs + laser groups, with drug concentrations of 60 $\mu g\ mL^{-1}$ for A375 and 30 $\mu g\ mL^{-1}$ for SK-Mel-28. A linear scratch was generated using a sterile pipette tip, and initial wound images were acquired using an inverted phase-contrast microscope (Zeiss, Germany). After 4 h of treatment, laser groups and PDA-Ce6-R837 NPs + laser groups were sequentially irradiated with 808 nm (60 s, 1 W cm^{-2}) and 660 nm (30 s, 0.05 W cm^{-2}). Wound closure was imaged after 24 h and quantified by measuring scratch width using Image J.

2.11 Transwell invasion assays

Invasive potential of A375 and SK-Mel-28 melanoma cells was evaluated using Matrigel-coated Transwell chambers. Cells were assigned to control (no treatment, no irradiation), laser (irradiation only), PDA-Ce6-R837 NPs, and PDA-Ce6-R837 NPs + laser groups, with drug concentrations of 60 $\mu g\ mL^{-1}$ for A375 and 30 $\mu g\ mL^{-1}$ for SK-Mel-28. Chambers were pre-coated with 1 : 32 Matrigel and incubated at 37 °C for 30 min. Cells were seeded in the upper chamber (2×10^5 cells per mL, 200 μL), with 800 μL of 10% FBS medium in the lower chamber, and incubated overnight. After 4 h treatment, laser groups and PDA-Ce6-R837 NPs + laser groups were irradiated at 808 nm (60 s, 1 W cm^{-2}) and 660 nm (30 s, 0.05 W cm^{-2}). The upper chamber medium was replaced with serum-free medium and the lower chamber with 15% FBS medium for overnight incubation. Chambers were washed, fixed with 4% paraformaldehyde for 20 min, stained with crystal violet for 5 min, and invasive cells were imaged with an upright optical microscope (Zeiss, Germany) and quantified using Image J.

2.12 Tumor cell apoptosis assays

Tumor cell apoptosis was evaluated in A375 and SK-Mel-28 melanoma cells, assigned to control (no treatment, no irradiation), laser (irradiation only), PDA-Ce6-R837 NPs, and PDA-Ce6-R837 NPs + laser groups, with drug concentrations of 60 $\mu g\ mL^{-1}$ for A375 and 30 $\mu g\ mL^{-1}$ for SK-Mel-28. Cells were seeded at 2×10^5 cells per mL in 12-well plates and allowed to adhere overnight. Following a 4 h incubation with the respective treatments, cells in the laser groups and PDA-Ce6-R837 NPs + laser groups were sequentially irradiated at 808 nm (60 s, 1 W cm^{-2}) and 660 nm (30 s, 0.05 W cm^{-2}). Both supernatant and adherent cells were collected, enzymatically detached using trypsin, resuspended in PBS. Annexin V staining was performed according to the manufacture's instructions, followed by PI addition immediately prior to analysis. Apoptotic populations were quantified using a flow cytometer (Beckman Coulter, USA) and analyzed with Flow Jo software.

2.13 Immunofluorescence staining

CRT exposure was analyzed by immunofluorescence staining. A375 and SK-Mel-28 melanoma cells were divided into control (no treatment, no irradiation), laser (irradiation only), PDA-Ce6-R837 NPs, and PDA-Ce6-R837 NPs + laser groups and seeded onto glass coverslips in 24-well plates at a density of 1.5×10^5 cells per mL. After 4 h treatment, laser groups and PDA-Ce6-

R837 NPs + laser groups received sequential irradiation at 808 nm (60 s, 1 W cm^{-2}) and 660 nm (30 s, 0.05 W cm^{-2}), followed by overnight incubation. Cells were then fixed, immunostained with anti-CRT primary and Alexa Fluor 488 conjugated secondary antibodies, and counterstained with Hoechst 33342. CRT localization was visualized using a confocal laser scanning microscope (Zeiss, Germany), and mean fluorescence intensity was quantified using Image J.

2.14 Measurement of extracellular ATP and HMGB1 release

Extracellular ATP and HMGB1 release were evaluated in A375 and SK-Mel-28 melanoma cells. Cells were seeded at 1 × 10^6 cells per mL in 6-well plates and assigned to control (no treatment, no irradiation), laser (irradiation only), PDA-Ce6-R837 NPs, and PDA-Ce6-R837 NPs + laser groups. After 4 h incubation with the respective treatments, laser groups and PDA-Ce6-R837 NPs + laser groups were sequentially irradiated with 808 nm (60 s, 1 W cm^{-2}) and 660 nm (30 s, 0.05 W cm^{-2}), followed by an additional 24 h incubation. Supernatants were collected to assess extracellular ATP using ATP Assay Kit, with samples and standards sequentially incubated with the kit reagents in a 37 °C water bath, followed by addition of the colorimetric substrate and absorbance measurement at 700 nm (Thermo Scientific, USA). HMGB1 levels were quantified in parallel using a commercial ELISA kit, with samples and standards added to antibody-coated wells, incubated, washed, treated with HRP-conjugated detection antibody and substrate, and absorbance read at 450 nm to determine concentrations from a standard curve.

2.15 BMDC maturation induced by PDA-Ce6-R837 NPs

Female C57BL/6 mice (8–10 weeks old) were handled in strict accordance with the Guidelines for Care and Use of Laboratory Animals of Sichuan University. All animal experiments were reviewed and approved by the Experimental Animal Ethics Committee of West China Hospital, Sichuan University (Permit Number: 20260126005). Mice were euthanized *via* cervical dislocation, and femurs and tibias were harvested. After removing adherent tissues, bones were rinsed with 75% ethanol and RPMI 1640 complete medium, and bone marrow was repeatedly flushed and filtered. Collected marrow cells were centrifuged, resuspended in RPMI 1640 containing 10% FBS at 2 × 10^6 cells per mL, and plated in 10 cm culture dishes with 20 ng mL^{-1} GM-CSF. On day 3, the medium was supplemented with GM-CSF (20 ng mL^{-1}) and IL-4 (10 ng mL^{-1}), and on day 6, the medium was replaced to ensure uniform cell distribution. On day 8, floating cells were harvested, resuspended in GM-CSF/IL-4 medium, and seeded into 12-well plates for subsequent assays.

To assess PDA-Ce6-R837 NPs induced maturation of BMDCs, A375 and SK-Mel-28 cells were allocated to control (no treatment, no irradiation), laser (irradiation only), R837 (60 μg mL^{-1} for A375; 30 μg mL^{-1} for SK-Mel-28), PDA-Ce6-R837 NPs, and PDA-Ce6-R837 NPs + laser groups (60 μg mL^{-1} for A375; 30 μg mL^{-1} for SK-Mel-28). Cells were seeded at 2 × 10^5 cells per mL in 12-well plates, allowed to adhere overnight, and treated for 4 h. Laser groups and PDA-Ce6-R837 NPs + laser groups were sequentially irradiated with 808 nm (60 s, 1 W cm^{-2}) and 660 nm (30 s, 0.05 W cm^{-2}) lasers, then cultured for an additional 24 h. Supernatants (100 μL) from each group were added to BMDCs and incubated overnight. A Blank group was included in which BMDCs were cultured without the addition of tumor cell supernatant. BMDCs were subsequently resuspended at 1 × 10^6 cells per mL in antibody dilution buffer, stained with CD80 and CD86 (1 : 100) and CD11c (1 : 200) fluorescent antibodies on ice for 1 h in the dark, washed, and analyzed for maturation marker expression using a flow cytometer (Beckman Coulter, USA). IL-12p70 levels in BMDCs culture supernatants were quantified *via* ELISA according to the manufacturer's instructions, with concentrations calculated from a standard curve.

2.16 Statistical analysis

Each experiment was repeated at least three times. Data are presented as mean ± SD and analyzed with GraphPad Prism 10.0 and Origin 2024. Statistical comparisons between two groups were performed using an unpaired two-tailed Student's *t*-test, while comparisons among multiple groups were conducted using one-way analysis of variance (ANOVA) followed by appropriate post hoc tests, with significance indicated as follows: $*p < 0.05$, $**p < 0.01$, $***p < 0.001$, $****p < 0.0001$.

3. Results

3.1 Characterization of PDA-Ce6-R837 NPs

To characterize the physicochemical properties of the nanoparticles, a series of structural and functional analyses were performed. As shown in Fig. 1A, SEM and TEM images reveal that PDA NPs have a regular spherical shape, smooth surface, and good dispersion, while PDA-Ce6-R837 NPs maintain a spherical shape but exhibit a rough surface and slightly larger particle size, indicating successful drug incorporation. After calculation, the EE of Ce6 and R837 was 82.3 ± 1.2% and 61.5 ± 1.0%, respectively, while the corresponding LE were 24.6 ± 0.8% and 11.4 ± 0.7%. In Fig. 1B, the UV-Vis absorption spectrum shows new absorption peaks at 260 nm, 400 nm, and 660 nm, confirming the successful integration of Ce6 and R837 into PDA-Ce6-R837 NPs. FTIR analysis (Fig. 1C) shows that the C=O stretching peak of Ce6 at 1707 cm^{-1} shifts to 1712 cm^{-1} in PDA-Ce6, indicating changes in the chemical environment likely due to π–π stacking and hydrogen bonding between PDA and Ce6. The characteristic peaks of R837 at 1645 cm^{-1} and 1578 cm^{-1} are preserved in PDA-R837 and PDA-Ce6-R837, confirming successful incorporation. XPS analysis (Fig. 1D–G) identifies the presence of C, N, and O elements, with the C 1s spectrum showing peaks for C–C (284.8 eV), C–O/C–N (286.0 eV), and C=O (288.0 eV). The N 1s spectrum shows peaks for C–N and N–H bonds, indicating nitrogen-containing groups. The O 1s spectrum shows peaks at 531–533 eV, corresponding to C=O and C–O bonds. As shown in Fig. 1H, the particle size of PDA-Ce6-R837 NPs remains stable over 4 days, indicating good colloidal stability. Fig. 1I and J show that, under laser

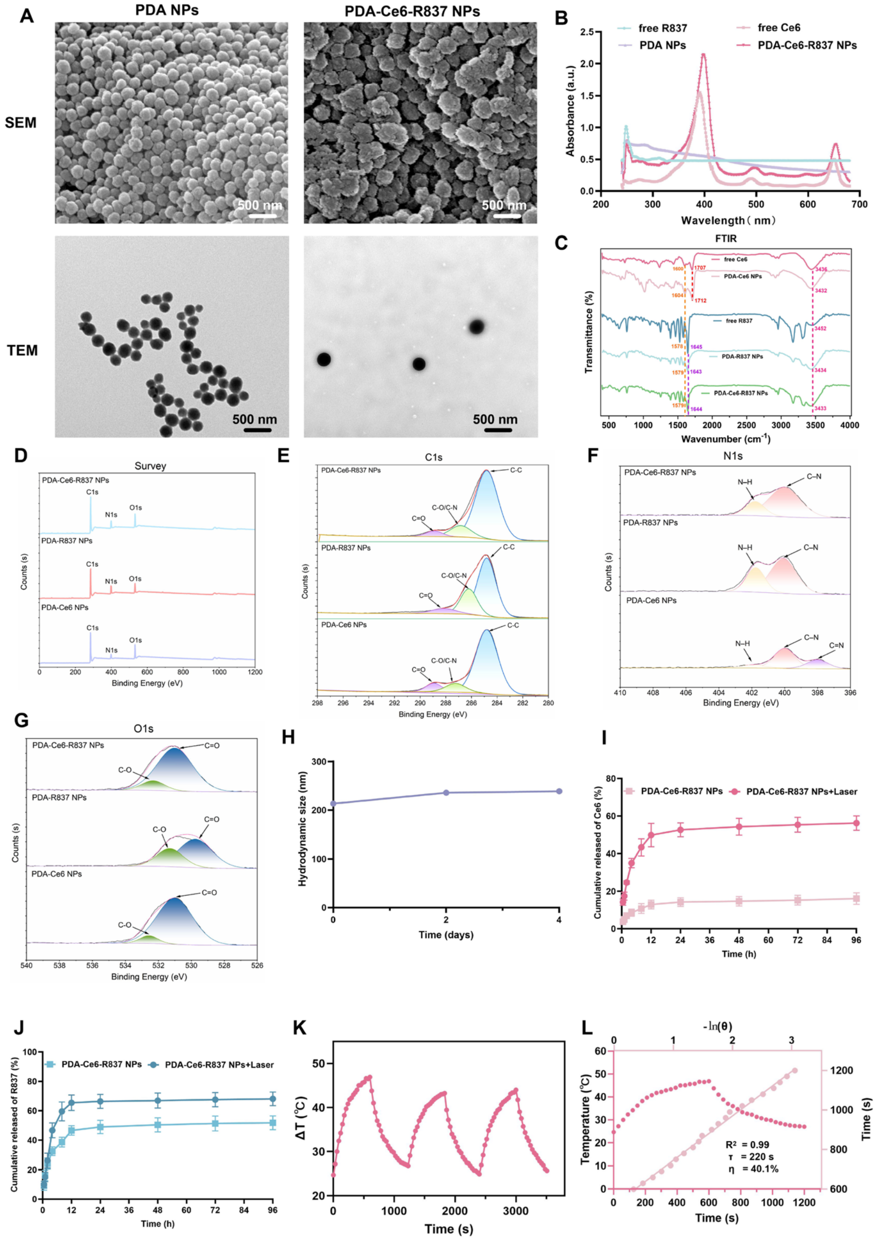

Fig. 1 Characterization of PDA-Ce6-R837 NPs. (A) SEM and TEM images showing the morphology of PDA NPs and PDA-Ce6-R837 NPs. (B) UV-Vis absorption spectra of PDA-Ce6-R837 NPs. (C) FTIR spectra of free Ce6, PDA-Ce6 NPs, free R837, PDA-R837 NPs and PDA-Ce6-R837 NPs showing characteristic peaks. (D–G) XPS spectra showing the elemental composition of PDA-Ce6-R837 NPs. (H) Particle size stability of PDA-Ce6-R837 NPs over 4 days. Drug release profiles of Ce6 (*I*) and R837 (*J*) under laser irradiation and without. Values represent the mean ± SD, $n = 3$. (K) Temperature rise and (L) photothermal conversion efficiency η of PDA-Ce6-R837 NPs under laser irradiation.

irradiation, Ce6 and R837 release efficiencies are 58.9% and 73.1%, respectively, significantly higher than without laser irradiation (14.9% and 56.3%). Fig. 1K shows that PDA-Ce6-R837 NPs reached a maximum temperature of 46.9 °C under laser irradiation and demonstrated stable thermal behavior over three heating/cooling cycles, with a calculated photothermal conversion efficiency η of 40.1% (Fig. 1L). These results validate the successful construction of PDA-Ce6-R837 NPs with desirable structural features, stability, light-responsive drug release, and favorable photothermal properties, providing a basis for subsequent *in vitro* evaluation of their photoimmunotherapeutic effects.

3.2 PDA-Ce6-R837 NPs induce PTT and PDT effects in melanoma cells

To evaluate the PTT and PDT therapeutic efficacy of PDA-Ce6-R837 NPs in melanoma cells, cellular uptake was first assessed by fluorescence imaging based on the intrinsic fluorescence of Ce6. Fluorescence imaging demonstrated efficient internalization of PDA-Ce6-R837 NPs in both A375 and SK-Mel-28 melanoma cells (Fig. 2A). Subsequently, cytotoxicity was evaluated using CCK-8 assays, which demonstrated a clear concentration-dependent decrease in cell viability following treatment with PDA-Ce6-R837 NPs (Fig. 2B and C). Based on

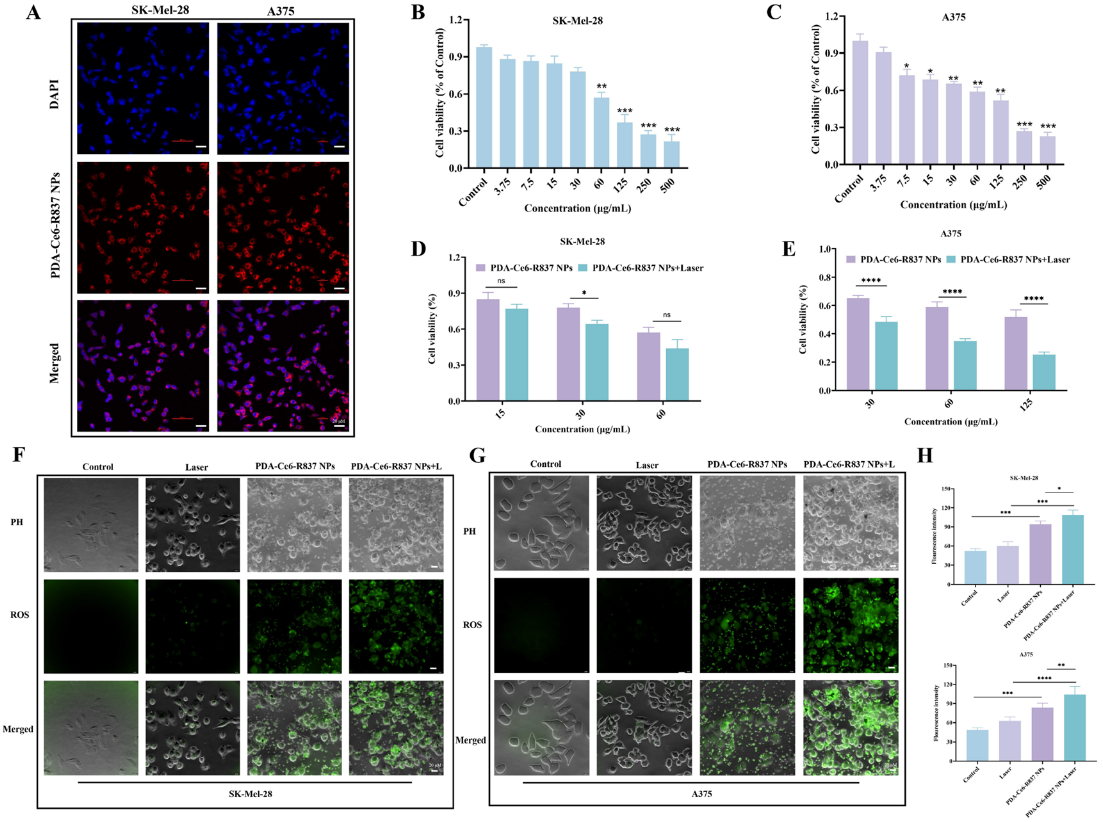

Fig. 2 PDA-Ce6-R837 NPs induce PTT and PDT effects in melanoma cells. (A) Fluorescence imaging demonstrating the cellular uptake of PDA-Ce6-R837 NPs by SK-Mel-28 and A375 cells. Cell viability of SK-Mel-28 (B) and A375 (C) cells following treatment with increasing concentrations of PDA-Ce6-R837 NPs, as assessed by the CCK-8 assay. Values represent the mean ± SD, $n = 3$. $^{*}p < 0.05$, $^{**}p < 0.01$, $^{***}p < 0.001$, compared with Control group. CCK-8 analysis of the effects of PDA-Ce6-R837 NPs at different concentrations on the viability of SK-Mel-28 (D) and A375 (E) cells in the presence or absence of laser irradiation. Intracellular ROS production in SK-Mel-28 (F) and A375 (G) cells after PDA-Ce6-R837 NPs treatment with or without laser irradiation. (H) Quantitative analysis of ROS levels. Values represent the mean ± SD, $n = 3$. $^{*}p < 0.05$, $^{**}p < 0.01$, $^{***}p < 0.001$, $^{****}p < 0.0001$.

these findings, concentrations that maintained at least 50% cell viability were selected for subsequent experiments. Upon dual-wavelength laser irradiation, PDA-Ce6-R837 NPs induced pronounced photothermal and photodynamic effects, with optimal responses observed at concentrations of 30 μg mL^{-1} in SK-Mel-28 cells and 60 μg mL^{-1} in A375 cells (Fig. 2D and E). In parallel, intracellular ROS generation was markedly elevated following combined treatment with PDA-Ce6-R837 NPs and laser irradiation, indicating potent photodynamic activity (Fig. 2F–H). Taken together, these results indicate that PDA-Ce6-R837 NPs are efficiently internalized by melanoma cells and can exert both photothermal and photodynamic effects under the present experimental conditions, providing a basis for further investigation of their dual-modal phototherapeutic potential.

3.3 PDA-Ce6-R837 NPs mediated phototherapy suppresses melanoma cells migration and invasion

The effects of PDA-Ce6-R837 NP-mediated phototherapy on melanoma cell migratory and invasive behaviors were further evaluated, given that enhanced migration and invasion are characteristic features of melanoma aggressiveness and metastatic progression. Wound healing assays revealed that laser-activated PDA-Ce6-R837 NPs markedly suppressed the migratory behavior of SK-Mel-28 cells, as evidenced by significantly delayed wound closure at 24 h compared with both control and non-laser irradiated conditions, while PDA-Ce6-R837 NPs alone also reduced cell migration relative to control (Fig. 3A and B). A comparable inhibitory effect on cell migration was observed in A375 cells (Fig. 3C and D), indicating that this response is not cell line-specific. Consistent with these findings, Transwell invasion assays demonstrated a pronounced reduction in invasive capacity following combined PDA-Ce6-R837 NPs treatment and laser irradiation in both melanoma models (Fig. 3E and F). Together, these results suggest that PDA-Ce6-R837 NPs-mediated phototherapy can suppress key functional features associated with melanoma aggressiveness, thereby providing a favorable biological context for the subsequent induction of ICD and immune activation-related processes.

3.4 PDA-Ce6-R837 NPs mediated phototherapy induces apoptosis in melanoma cells

Apoptosis induction, which is essential for ICD initiation through the release of immunogenic danger-associated

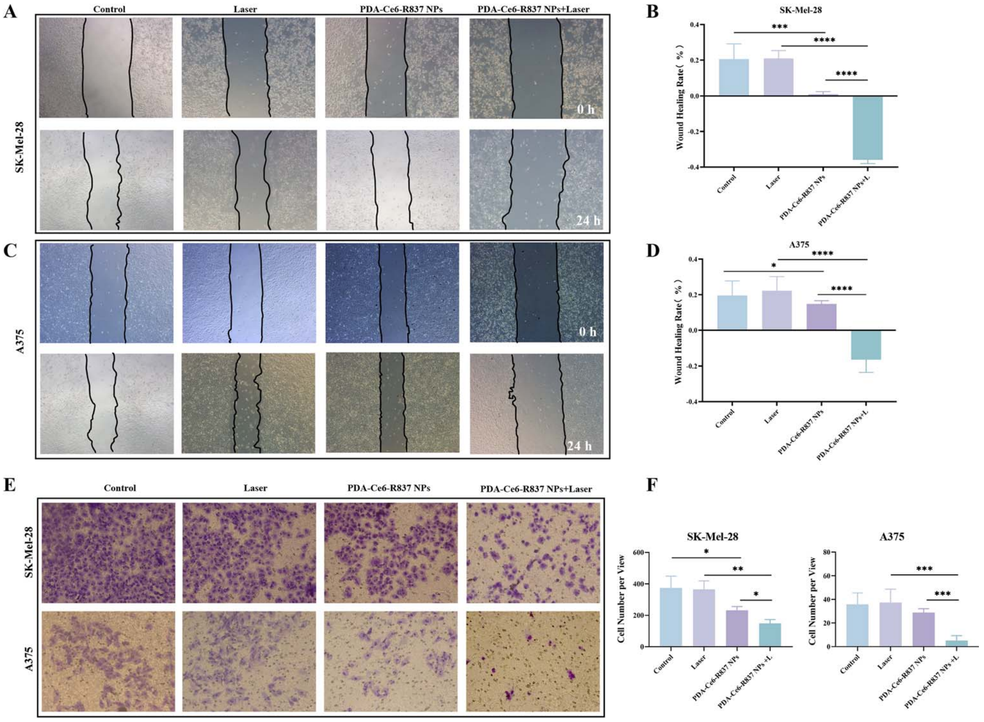

Fig. 3 PDA-Ce6-R837 NPs mediated phototherapy suppresses melanoma cells migration and invasion. (A) Representative images of wound healing assays in SK-Mel-28 cells treated with PDA-Ce6-R837 NPs with or without laser irradiation at 0 h and 24 h. (B) Quantitative analysis of wound closure in SK-Mel-28 cells under the indicated treatment conditions. (C) Representative images of wound healing assays in A375 cells treated with PDA-Ce6-R837 NPs with or without laser irradiation at 0 h and 24 h. (D) Quantitative analysis of wound closure in A375 cells under the indicated treatment conditions. (E) Representative images of Transwell invasion assays showing the invasive behavior of melanoma cells under different treatments. (F) Quantification of invaded SK-Mel-28 and A375 cells following PDA-Ce6-R837 NPs mediated phototherapy. All values represent the mean ± SD, $n = 3$. *$p < 0.05$, **$p < 0.01$, ***$p < 0.001$, ****$p < 0.0001$.

molecules, was further evaluated following PDA-Ce6-R837 NP-mediated phototherapy.[49] As shown in Fig. 4A–C, laser irradiation alone induced minimal apoptotic responses in both A375 and SK-Mel-28 cells compared with the control group. Treatment with PDA-Ce6-R837 NPs significantly increased apoptosis rates in both melanoma cell lines. Dual-wavelength laser irradiation combined with PDA-Ce6-R837 NPs treatment further enhanced apoptotic responses, yielding the highest apoptosis levels in both cell lines compared with all single-treatment groups. Collectively, these results suggest that PDA-Ce6-R837 NPs mediated phototherapy promotes melanoma cell apoptosis, thereby providing a cellular basis for the subsequent induction of ICD processes.

3.5 PDA-Ce6-R837 NPs mediated phototherapy induces ICD in melanoma cells

The ability of PDA-Ce6-R837 NP-mediated phototherapy to induce ICD in melanoma cells was evaluated by analyzing the exposure and release of DAMPs. Under basal conditions, CRT, a key "eat-me" signal of ICD, is primarily localized to the endoplasmic reticulum and the nuclear envelope, from where it translocates to the cell surface to mediate immune recognition of dying tumor cells.[50,51] Immunofluorescence analysis revealed that in A375 cells, CRT was predominantly localized around the nuclear envelope under basal conditions, whereas combined PDA-Ce6-R837 NPs treatment and laser irradiation induced pronounced CRT externalization and colocalization with Ce6 fluorescence, yielding a markedly enhanced surface-associated signal relative to control and non-irradiated groups (Fig. 5A). A similar treatment-dependent increase in membrane-associated CRT fluorescence was observed in SK-Mel-28 cells, where CRT is primarily distributed within the endoplasmic reticulum (Fig. 5B). Fluorescence intensity analysis confirmed a significant elevation of CRT expression in the laser-activated PDA-Ce6-R837 NPs group compared with all other groups (Fig. 5C). Consistent with these findings, extracellular release of ATP and HMGB1—additional molecular hallmarks of ICD—was significantly increased following PDA-Ce6-R837 NPs treatment and further amplified upon laser irradiation (Fig. 5D and E). Together, these results suggest that laser-activated PDA-Ce6-R837 NPs can induce ICD-associated molecular signals in melanoma cells, thereby providing a favorable context for subsequent dendritic cell maturation.

3.6 Dual-mechanism promotion of BMDC maturation by PDA-Ce6-R837 NPs

The effects of PDA-Ce6-R837 NPs treatment on bone marrow-derived dendritic cells (BMDCs) activation were evaluated by measuring the expression of CD80 and CD86 and the secretion of IL-12p70. Flow cytometric analysis revealed that coculture

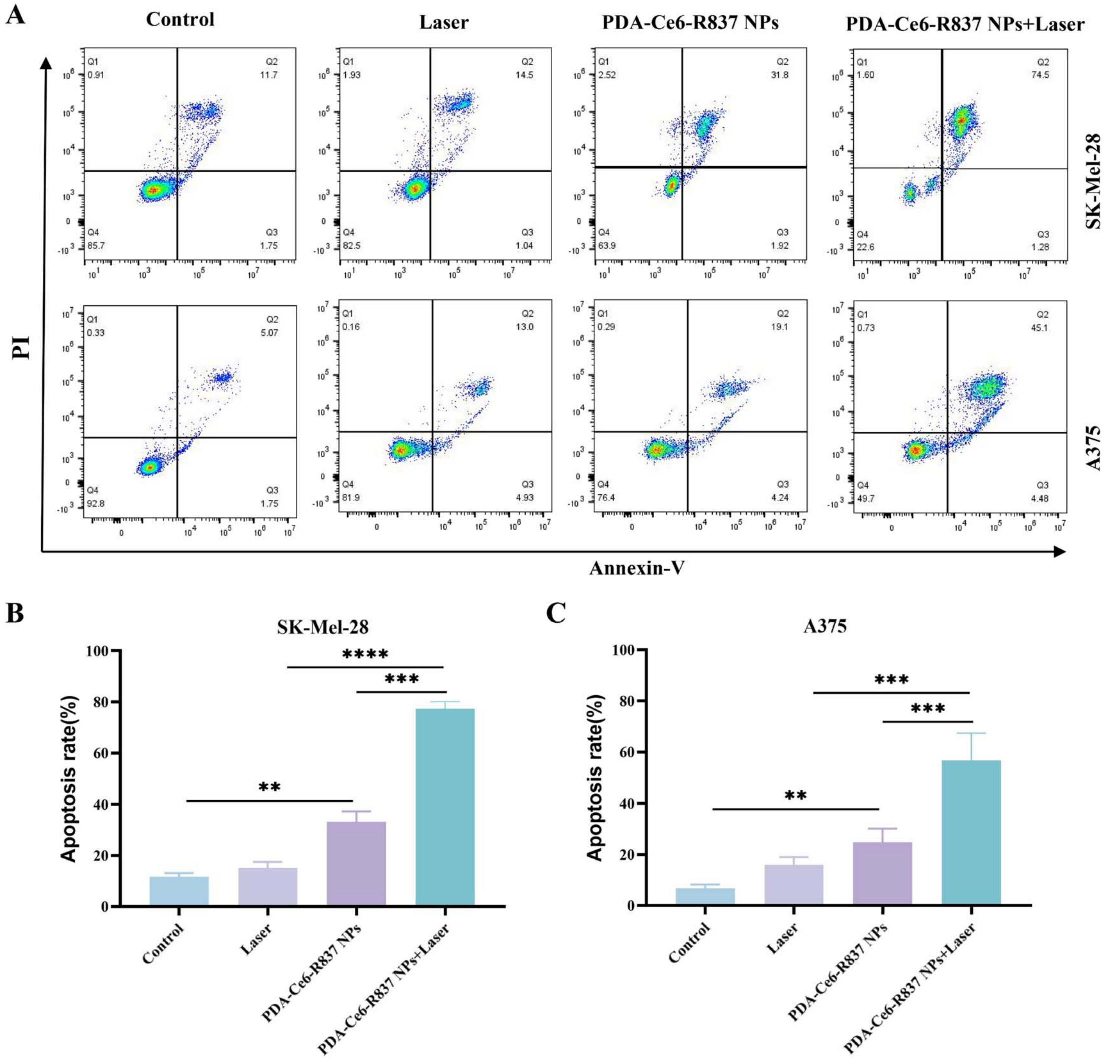

Fig. 4 PDA-Ce6-R837 NPs mediated phototherapy induces apoptosis in melanoma cells. (A) Representative flow cytometry plots showing apoptosis in SK-Mel-28 and A375 cells following different treatments. Quantitative analysis of apoptotic rates in SK-Mel-28 (B) and A375 (C) cells under indicated conditions. All values represent the mean ± SD, $n = 3$. $^{**}p < 0.01$, $^{***}p < 0.001$, $^{****}p < 0.0001$.

with melanoma cells treated with R837 alone modestly increased the fraction of CD80$^+$/CD86$^+$ BMDCs, relative to the control, confirming the intrinsic adjuvant activity of R837. Notably, treatment with PDA-Ce6-R837 NPs further amplified BMDC maturation, suggesting efficient delivery and sustained bioactivity of the encapsulated R837. This effect was substantially enhanced by laser irradiation, which led to the highest proportion of mature BMDCs observed in both SK-Mel-28 and A375 cell models (Fig. 6A and B). In parallel, IL-12p70 secretion in BMDCs cultures was significantly elevated following treatment with either R837 or PDA-Ce6-R837 NPs, with laser activation inducing an additional surge in IL-12p70 production (Fig. 6C), confirming functional maturation of the BMDCs. Together, these findings suggest that PDA-Ce6-R837 NPs promote BMDC activation through two complementary pathways: phototherapy-induced ICD provides tumor-associated immunogenic signals, while R837 functions as an immune adjuvant that directly enhances BMDCs maturation. This photo-immunotherapeutic strategy may contribute to immune activation and provide a basis for further investigation of phototherapy-based immunotherapeutic approaches.

4. Discussion

Melanoma exhibits pronounced heterogeneity and intrinsic resistance to conventional therapies, presenting a formidable challenge for monotherapeutic approaches.[52,53] To overcome these limitations, multifunctional nanoplatforms that integrate complementary therapeutic modalities offer a promising strategy for advanced melanoma management. Building on our previous work, we developed a PDA-based nanoparticle capable of co-delivering the Ce6 and R837 (PDA-Ce6-R837 NPs).[46] Here, we systematically investigated the antitumor efficacy of PDA-Ce6-R837 NPs in melanoma cell models and evaluated their capacity to trigger ICD and potentiate antitumor immune responses.

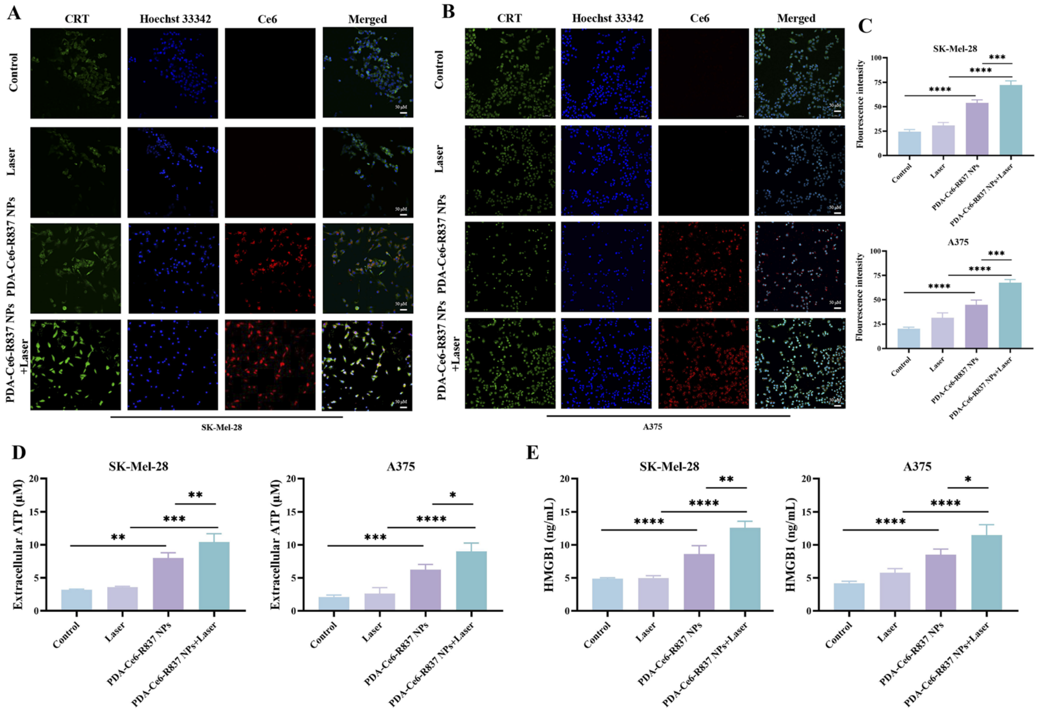

Fig. 5 PDA-Ce6-R837 NPs mediated phototherapy induces ICD in melanoma cells. Immunofluorescence staining of CRT in SK-Mel-28 (A) and A375 (B) cells under basal conditions or following treatment with PDA-Ce6-R837 NPs with or without laser irradiation. (C) Quantification of membrane-associated CRT fluorescence intensity after treatment. Measurement of extracellular ATP (D) and HMGB1 (E) release in response to PDA-Ce6-R837 NPs with or without laser irradiation. Scale bar = 50 μm. All values represent the mean ± SD, $n = 3$. *$p < 0.05$, **$p < 0.01$, ***$p < 0.001$, ****$p < 0.0001$.

Recent studies have highlighted that the performance of phototherapy-based nanoplatforms depends not only on their photophysical properties, but also on efficient cellular uptake and intracellular localization, which directly influence ROS generation, local thermal effects, and the resulting biological responses.[54–56] Thus, efficient cellular uptake and controlled

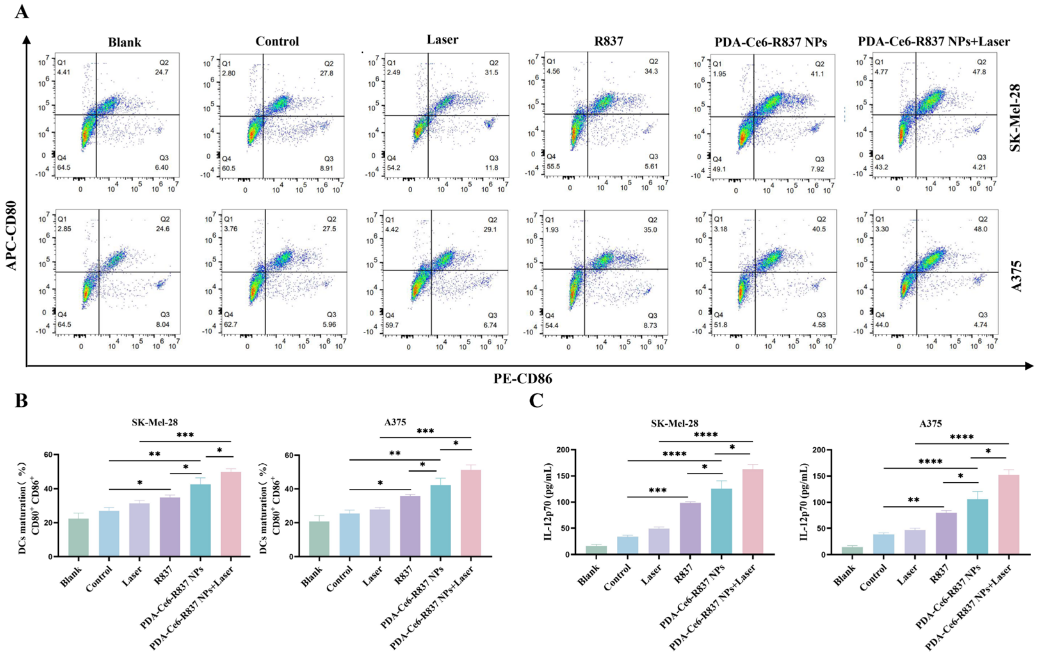

Fig. 6 Dual-mechanism promotion of BMDC maturation by PDA-Ce6-R837 NPs. (A) Flow cytometry analysis of surface maturation markers CD80 and CD86 in BMDCs. (B) The proportion of $CD80^+CD86^+$ double-positive cells is shown. (C) IL-12p70 secretion in BMDCs culture supernatants was measured by ELISA. All values represent the mean ± SD, $n = 3$. *$p < 0.05$, **$p < 0.01$, ***$p < 0.001$, ****$p < 0.0001$.

intracellular distribution are pivotal for achieving effective PDT/PTT responses. In this study, PDA-Ce6-R837 NPs were robustly internalized by SK-Mel-28 and A375 melanoma cells, providing a mechanistic basis for their combined photodynamic and photothermal activity. Previous studies have suggested that PDA-based systems may interact with cell-surface receptors, and PDA receptor signaling has also been implicated in melanoma biology.[57–59] In the present study, although efficient cellular uptake of PDA-Ce6-R837 NPs was observed, the specific uptake pathway was not directly investigated. Therefore, the possible involvement of receptor-related mechanisms should be regarded as a tentative interpretation rather than a demonstrated conclusion.

In vitro evaluation of PDA-Ce6-R837 NPs revealed dose-dependent cytotoxicity in SK-Mel-28 and A375 melanoma cells even in the absence of laser irradiation. Upon dual-laser irradiation, the tumoricidal effect was markedly enhanced, likely due to the combined contribution of multiple mechanisms. Specifically, laser exposure induces structural changes in PDA, weakening its interactions with Ce6 and R837 and facilitating rapid drug release. At the same time, laser activation triggers concurrent photothermal and photodynamic effects, which together amplify tumor cell killing. This interplay between PDT and PTT is well supported by extensive evidence demonstrating enhanced antitumor efficacy at the cellular level.[54] Hyperthermia sensitizes tumor cells to PDT-induced death by denaturing DNA repair proteins, thereby diminishing their capacity to recover from sublethal damage.[60] Concurrently, PTT-generated heat promotes intracellular delivery and retention of photosensitizers, further potentiating PDT efficacy. Elevated temperatures also increase mitochondrial ROS, amplifying oxidative stress, while PDT-mediated impairment of heat shock proteins compromises their cytoprotective function, thereby reinforcing the combined cytotoxic effect of PTT and PDT.[61] Collectively, the combined photodynamic and photothermal effects may contribute to both tumor cell cytotoxicity and microenvironment-related changes, providing a possible explanation for the enhanced tumor cell killing observed under dual-laser irradiation of PDA-Ce6-R837 NPs.

ICD represents a specialized form of programmed cell death, defined by hallmark signals such as CRT surface exposure and the extracellular release of ATP and HMGB1.[62] These DAMPs are readily detected and internalized by BMDCs, driving their phenotypic and functional maturation and providing critical cues for the initiation of T cell-mediated antitumor immunity.[63] However, many recent studies have primarily focused on nanoplatform construction and cytotoxic or phototherapeutic efficacy in melanoma models, whereas the *in vitro* photo-immunological responses, particularly those linking tumor cell damage to ICD-associated signaling and dendritic cell activation, remain to be further clarified.[64–66] Remarkably, PDA-Ce6-R837 NPs elicited measurable ICD features even in the absence of laser irradiation, as indicated by elevated CRT exposure and ATP/HMGB1 release compared with controls in this study. This basal activity likely reflects the intrinsic immunomodulatory effects of R837 coupled with its sustained release from the PDA carrier, which induces cellular stress responses. Furthermore, although R837 was shown to directly

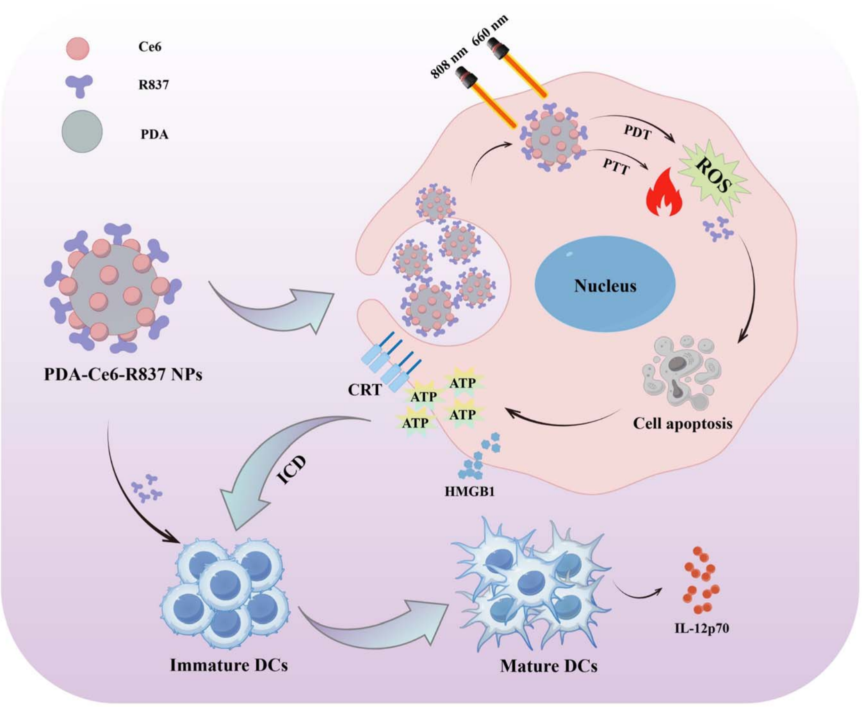

Fig. 7 Schematic illustration of PDA-Ce6-R837 NP-mediated photo-immunotherapy. Intracellular PDA-Ce6-R837 NPs activation under dual-wavelength laser irradiation (808 nm and 660 nm) triggers therapeutic agent release, leading to ICD and subsequent DAMPs signaling. This process promotes maturation of immature DCs and stimulates IL-12p70-mediated antitumor immune activation.

promote BMDC maturation in this study, its specific contribution within the integrated nanoplatform, as well as its effects on melanoma cells themselves, was not systematically dissected and should be further clarified in future work. Collectively, these results demonstrate that PDA-Ce6-R837 NPs possess inherent immunostimulatory functionality, while photothermal–photodynamic activation augments their therapeutic potential, establishing a dual strategy of baseline cytotoxicity and light-enhanced immunogenicity. Mechanistically, these effects likely arise from efficient intracellular nanoparticle accumulation, photodynamically generated ROS, and photothermal-induced protein denaturation, which together lower the threshold for ICD induction and facilitate robust release of immunostimulatory signals from tumor cells (Fig. 7).

Overall, PDA-Ce6-R837 NPs-mediated phototherapy suppressed key functional traits associated with melanoma malignancy, including proliferation, migration, invasion, and apoptosis resistance, while also being associated with ICD-related signals and BMDC activation. These findings suggest that this nanoplatform may serve as a useful *in vitro* model for studying the link between phototherapy-induced tumor damage and immune activation-related processes. It should be noted, however, that all experiments in this study were conducted *in vitro*; therefore, further *in vivo* studies are required to validate the therapeutic relevance and associated immune responses. Nevertheless, the present study provides preliminary *in vitro* evidence for future investigations of integrated phototherapy–immunotherapy strategies in melanoma.

5. Conclusion

In conclusion, PDA-Ce6-R837 NPs were found to exhibit dose-dependent cytotoxicity in SK-Mel-28 and A375 melanoma cells, with enhanced cytotoxic effects under dual-laser irradiation. PDA-Ce6-R837 NPs-mediated phototherapy significantly inhibited cell migration and invasion and induced apoptosis, along with key features of immunogenic cell death (ICD), including CRT exposure and the release of ATP and HMGB1. Additionally, these effects were associated with enhanced BMDC maturation and increased IL-12p70 secretion. These findings suggest that PDA-Ce6-R837 NPs can induce tumor cell damage while being associated with immune activation-related processes. This study provides *in vitro* evidence for the further investigation of PDA-Ce6-R837 NPs in phototherapy-based immunotherapeutic strategies and offers a basis for future *in vivo* evaluation in melanoma models.

Author contributions

J. W.: formal analysis, methodology, writing – original draft, writing – review & editing; C. L.: formal analysis, methodology, writing – original draft, writing – review & editing; X. Z.: formal analysis, methodology, writing – original draft, writing – review & editing; Y. X.: methodology, funding acquisition, project administration; X. Z.: methodology; T. W.: conceptualization, methodology, project administration, supervision; L. W.: conceptualization, methodology, project administration, supervision and writing – review & editing.

Conflicts of interest

The authors declare that they have no known competing financial interests or personal relationships that could have appeared to influence the work reported in this paper.

Data availability

The data supporting the findings of this study are included in the article.

Acknowledgements

We thank Fig.draw (https://www.Fig.draw.com) for the assistance in creating Fig. 7. This work was supported by the Sichuan Science and Technology Program (2024NSFSC1627) and the Cross-disciplinary Innovation Project of the 135 Project for the Outstanding Development of Disciplines at West China Hospital, Sichuan University (ZYJC21051).

References

1 W. H. Ward and J. M. Farma, *Cutaneous Melanoma: Etiology and Therapy*, Exon Publications, Australia, 2017.
2 F. Feng, Y. Ma, Y. Zhao, Z. Wan, R. Zhang and S. Yang, *Sci. Rep.*, 2025, **15**, 39300.
3 A. C. Huang and R. Zappasodi, *Nat. Immunol.*, 2022, **23**, 660–670.
4 T. Amaral, M. Ottaviano, A. Arance, C. Blank, V. Chiarion-Sileni, M. Donia, R. Dummer, C. Garbe, J. E. Gershenwald, H. Gogas, M. Guckenberger, J. Haanen, O. Hamid, A. Hauschild, C. Höller, C. Lebbé, R. J. Lee, G. V. Long, P. Lorigan, E. Muñoz Couselo, P. Nathan, C. Robert, E. Romano, D. Schadendorf, V. Sondak, K. P. M. Suijkerbuijk, A. C. J. van Akkooi and O. Michielin, *Ann. Oncol.*, 2025, **36**, 10–30.
5 J. D. Wolchok, V. Chiarion-Sileni, P. Rutkowski, C. L. Cowey, D. Schadendorf, J. Wagstaff, P. Queirolo, R. Dummer, M. O. Butler, A. G. Hill, M. A. Postow, C. Gaudy-Marqueste, T. Medina, C. D. Lao, J. Walker, I. Márquez-Rodas, J. B. A. G. Haanen, M. Guidoboni, M. Maio, P. Sch Ffski, M. S. Carlino, S. Sandhu, C. Lebbé, P. A. Ascierto, G. V. Long, C. Ritchings, A. Nassar, M. Askelson, M. P. Benito, W. Wang, F. S. Hodi, J. Larkin and I. Checkmate, *N. Engl. J. Med.*, 2025, **392**, 11–22.
6 A. Takahashi, K. Namikawa, D. Ogata, E. Nakano, S. Jinnai, K. Nakama, K. Tsutsui, Y. Muto, H. Mizuta and N. Yamazaki, *J. Dermatol.*, 2020, **47**, 1267–1275.
7 S. Premi, Y. Qin and N. Ahmad, *Front. Oncol.*, 2022, **12**, 1016901.
8 J. Lu, R. He, Y. Liu, J. Zhang, H. Xu, T. Zhang, L. Chen, G. Yang, J. Zhang, J. Liu and H. Chi, *Front. Cell Dev. Biol.*, 2024, **12**, 1416115.

9 J. Zhang, X. Shi, M. Wang, R. Zhai, M. Wang, Z. Gong, Z. Ni, T. Xu, W. Zhu and L. Liu, *J. Cancer Res. Clin. Oncol.*, 2024, **150**, 240.

10 K. Fang, S. Yuan, X. Zhang, J. Zhang, S. Sun and X. Li, *Front. Immunol.*, 2025, **16**, 1571212.

11 S. Jafari, A. K. Ardakan, E. M. Aghdam, A. Mesbahi, S. Montazersaheb and O. Molavi, *Sci. Rep.*, 2024, **14**, 23231.

12 T. Moriya, K. Kitagawa, Y. Hayakawa, H. Hemmi, T. Kaisho, S. Ueha, R. Ikebuchi, I. Yasuda, Y. Nakanishi, T. Honda, K. Matsushima, K. Kabashima, M. Ueda, Y. Kusumoto, T. Chtanova and M. Tomura, *iScience*, 2021, **24**, 102424.

13 X. Qiao, P. Ma, J. Guo, Y. Sun, L. Peng, N. Yu, W. Zuo and J. Yang, *J. Mater. Chem. B*, 2025, **13**, 7401–7414.

14 L. Yu, P. Wang, Q. Shen, Q. Guan, Z. Li, Y. Han, X. Zhang, Q. Hu and C. Tan, *Adv. Sci.*, 2026, **13**, e14256.

15 Y. Zhang, P. Naderi Yeganeh, H. Zhang, S. Y. Wang, Z. Li, B. Gu, D. Lee, Z. Zhang, A. Ploumakis, M. Shi, H. Wu, E. L. Greer, W. Hide and J. Lieberman, *Nat. Immunol.*, 2024, **25**, 1858–1870.

16 H. Sui, S. Dongye, X. Liu, X. Xu, L. Wang, C. Q. Jin, M. Yao, Z. Gong, D. Jiang, K. Zhang, Y. Liu, H. Liu, G. Jiang and Y. Su, *Front. Immunol.*, 2022, **13**, 990463.

17 R. Malekzadeh, T. Mortezazadeh, W. K. Abdulsahib, B. Babaye Abdollahi, M. R. Hamblin, B. Mansoori, F. Alsaikhan and B. Zeng, *Environ. Res.*, 2023, **236**, 116526.

18 M. Wu, Y. Chang, T. Lin, C. Wu, J. Chang and Y. Lu, *Discover Nano*, 2025, **20**, 106.

19 S. Duan, Y. Hu, Y. Zhao, K. Tang, Z. Zhang, Z. Liu, Y. Wang, H. Guo, Y. Miao, H. Du, D. Yang, S. Li and J. Zhang, *RSC Adv.*, 2023, **13**, 14443–14460.

20 H. Shen, P. Xie, R. Yi, J. Zhou, S. Huang, L. Zhang, X. Huang, J. Zhao, S. Wang and C. Zhu, *J. Colloid Interface Sci.*, 2025, **694**, 137713.

21 A. Carmignani, M. Battaglini, A. Marino, F. Pignatelli and G. Ciofani, *ACS Appl. Bio Mater.*, 2024, **7**, 2205–2217.

22 J. Wang, Y. Wang, H. Song, X. Yang and Y. Zhang, *Eur. J. Pharm. Biopharm.*, 2026, 115046.

23 E. Nestoros, F. de Moliner, F. Nadal-Bufi, D. Seah, M. C. Ortega-Liebana, Z. Cheng, S. Benson, C. Adam, L. Maierhofer, K. Kozoriz, J. Lee, A. Unciti-Broceta and M. Vendrell, *Nat. Commun.*, 2024, **15**, 7689.

24 D. Aebisher, S. Czech, K. Dynarowicz, M. Misio Ek, K. Komosińska-Vassev, A. Kawczyk-Krupka and D. Bartusik-Aebisher, *Int. J. Mol. Sci.*, 2024, **25**, 11325.

25 P. H. Ahn, H. Quon, B. W. O Malley, G. Weinstein, A. Chalian, K. Malloy, J. H. Atkins, T. Sollecito, M. Greenberg, S. Mcnulty, A. Lin, T. C. Zhu, J. C. Finlay, K. Cengel, V. Livolsi, M. Feldman, R. Mick and T. M. Busch, *Oral Oncol.*, 2016, **55**, 37–42.

26 M. Sakamoto, S. Takeda, A. Fujiwara, M. Hirata, S. Hirose, K. Matsuoka, K. Umayahara, K. Iwaya, T. Tanaka and A. Okamoto, *Photodiagn. Photodyn. Ther.*, 2026, **58**, 105372.

27 H. Chen, H. Li, H. Li and Z. Zhang, *Front. Oncol.*, 2025, **15**, 1528314.

28 W. Aung, A. B. Tsuji, Z. Jin, A. Sugyo, C. Kajiwara and T. Higashi, *Technol. Cancer Res. Treat.*, 2025, **24**, 2050835116.

29 A. Hak, M. S. Ali, S. A. Sankaranarayanan, V. R. Shinde and A. K. Rengan, *ACS Appl. Bio Mater.*, 2023, **6**, 349–364.

30 O. P. Krivosheeva, M. A. Doctor, E. A. Larkina, A. S. Vedenkin and T. A. Nikolskaya, *Photodiagn. Photodyn. Ther.*, 2023, **42**, 103328.

31 J. He, G. Wang, Y. Zhou, B. Li and P. Shang, *Front. Bioeng. Biotechnol.*, 2025, **13**, 1553653.

32 K. X, W. Ali, Y. Chong, Z. Wang, L. Xue and F. Wang, *Int. J. Biol. Sci.*, 2026, **22**, 1560–1588.

33 Y. S. Birhan, C. Hsu, H. Yu and P. Lai, *Mater. Today Bio*, 2025, **31**, 101587.

34 D. Kan, R. Ding, H. Yang, Y. Jia, K. Lei, Z. Wang, W. Zhang, C. Yang, Z. Liu and F. Xie, *Front. Oncol.*, 2025, **15**, 1607259.

35 J. Liang, X. Lai, Y. Mei, X. Liu, S. Wen, Y. Zhou and F. Liu, *Int. J. Nanomed.*, 2026, **21**, 1–18.

36 S. Yasuda, Y. Horikawa, M. Ohashi, M. Amou, T. Kanamori, D. Runjing, Y. Tamemoto, W. Xu, T. Niidome, A. Hisaka and H. Hatakeyama, *Cancers*, 2026, **18**, 287.

37 L. Zhou, L. Chen, X. Hu, Y. Lu, W. Liu, Y. Sun, T. Yao, C. Dong and S. Shi, *Commun. Biol.*, 2020, **3**, 343.

38 J. Mondal, S. Prabha, T. S. Griffith, D. Ferguson and J. Panyam, *Cancers*, 2025, **17**, 3582.

39 B. C. Gilmour, A. Corthay and I. Ynebr Ten, *npj Vaccines*, 2024, **9**, 83.

40 M. Sanlorenzo, P. Novoszel, I. Vujic, T. Gastaldi, M. Hammer, O. Fari, C. De Sa Fernandes, A. D. Landau, B. V. G Cen-Oguz, M. Holcmann, B. Monshi, K. Rappersberger, A. Csiszar and M. Sibilia, *Nat. Cancer*, 2025, **6**, 175–193.

41 C. M. Fehres, S. C. M. Bruijns, A. J. van Beelen, H. Kalay, M. Ambrosini, E. Hooijberg, W. W. J. Unger, T. D. de Gruijl and Y. van Kooyk, *Eur. J. Immunol.*, 2014, **44**, 2415–2424.

42 M. A. Stanley, *Clin. Exp. Dermatol.*, 2002, **27**, 571–577.

43 L. Krajewska-W Glewicz, P. Sobolewski and I. Walecka, *Cancers*, 2025, **17**, 2111.

44 H. Jamshaid, F. U. Din, M. Malik, M. Mukhtiar, H. G. Choi, T. Ur-Rehman and G. M. Khan, *Sci. Rep.*, 2022, **12**, 14244.

45 F. Auderset, E. Belnoue, B. Mastelic-Gavillet, P. Lambert and C. Siegrist, *Front. Immunol.*, 2020, **11**, 580974.

46 X. Zhang, J. Zhu, T. Li, H. Cao and L. Wang, *J. Mater. Chem. B*, 2026, **14**, 234–247.

47 Y. Yang, D. Hu, Y. Lu, B. Chu, X. He, Y. Chen, Y. Xiao, C. Yang, K. Zhou, L. Yuan and Z. Qian, *Acta Pharm. Sin. B*, 2022, **12**, 2710–2730.

48 X. Zhao, H. Zhao, S. Wang, Z. Fan, Y. Ma, Y. Yin, W. Wang, R. Xi and M. Meng, *J. Am. Chem. Soc.*, 2021, **143**, 20828–20836.

49 D. R. Green, T. Ferguson, L. Zitvogel and G. Kroemer, *Nat. Rev. Immunol.*, 2009, **9**, 353–363.

50 J. Fucikova, R. Spisek, G. Kroemer and L. Galluzzi, *Cell Res.*, 2021, **31**, 5–16.

51 K. H. Krause and M. Michalak, *Cell*, 1997, **88**, 439–443.

52 B. M. Robertson, M. E. Fane, A. T. Weeraratna and V. W. Rebecca, *Nat. Cancer*, 2024, **5**, 964–982.

53 D. K Nig, M. T. Sandholzer, S. Uzun, A. Zingg, R. Ritschard, H. Thut, K. Glatz, E. A. Kappos, D. J. Schaefer, C. Kettelhack, J. R. Passweg, A. Holbro, K. Baur, M. Medinger, A. Buser,

D. Lardinois, L. T. Jeker, N. Khanna, F. Stenner, B. Kasenda, K. Homicsko, M. Matter, N. Rodrigues Mantuano, A. Zippelius and H. L. Ubli, *Cancer Immunol. Res.*, 2024, **12**, 814–821.

54 M. Overchuk, R. A. Weersink, B. C. Wilson and G. Zheng, *ACS Nano*, 2023, **17**, 7979–8003.

55 X. Zhang, J. Wang, S. Wang, L. Fu, X. Du, Q. Rong, C. Yao and J. Xin, *Int. J. Nanomed.*, 2025, **20**, 13661–13687.

56 M. Salimi, S. Mosca, B. Gardner, F. Palombo, P. Matousek and N. Stone, *Nanomaterials*, 2022, **12**, 922.

57 Y. Liu, C. K. K. Choi, H. Hong, Y. Xiao, M. L. Kwok, H. Liu, X. Y. Tian and C. H. J. Choi, *ACS Nano*, 2021, **15**, 13871–13890.

58 Z. Liang, Y. He, C. S. Ieong and C. H. J. Choi, *Curr. Opin. Biotechnol.*, 2023, **84**, 103013.

59 M. A. M. Peters, C. Meijer, R. S. N. Fehrmann, A. M. E. Walenkamp, I. P. Kema, E. G. E. de Vries, H. Hollema and S. F. Oosting, *Pathol. Oncol. Res.*, 2020, **26**, 1539–1547.

60 F. Kradolfer, C. Maake and B. Spingler, *Chem. Commun.*, 2025, **61**, 14757–14772.

61 H. Kurokawa, H. Ito, M. Terasaki and H. Matsui, *Sci. Rep.*, 2019, **9**, 1638.

62 I. Martins, Y. Wang, M. Michaud, Y. Ma, A. Q. Sukkurwala, S. Shen, O. Kepp, D. Métivier, L. Galluzzi, J. Perfettini, L. Zitvogel and G. Kroemer, *Cell Death Differ.*, 2014, **21**, 79–91.

63 Y. Guo, X. Zhang, S. Wang, H. Feng, S. Wu and F. Wu, *Research*, 2023, **6**, 52.

64 A. A. Obalola, H. Abrahamse and S. S. Dhilip Kumar, *ACS Omega*, 2026, **11**, 25004–25013.

65 L. Pires, S. Khattak, S. Pratavieira, C. Calcada, R. Romano, Y. Yucel, V. S. Bagnato, C. Kurachi and B. C. Wilson, *Proc. Natl. Acad. Sci. U. S. A.*, 2024, **121**, e1978664175.

66 S. S. Shabnum, R. Siranjeevi, C. K. Raj, A. Saravanan, A. S. Vickram, H. Chopra and T. Malik, *RSC Adv.*, 2024, **14**, 38952–38995.